Research Square

Preprints are preliminary reports that have not undergone peer review.
They should not be considered conclusive, used to inform clinical practice,
or referenced by the media as validated information.

Bridging human kidney stone dynamics and damage under shock-wave lithotripsy: synchrotron X-ray imaging and tomography

Cameron Brewer

cbrewer@ethz.ch

ETH Zurich

Armand Sieber

ETH Zurich https://orcid.org/0000-0002-9961-7312

Bratislav Lukic

ESRF The European Synchrotron

Gazendra Shakya

ETH Zurich

Guillaume Bokman

ETH Zurich

Markus Belau

Storz Medical AG https://orcid.org/0000-0002-7119-0177

Arvid Kühl

Storz Medical AG

Moritz Schlötter

Storz Medical AG https://orcid.org/0000-0002-1264-7704

Kevin Schmidmayer

Inria Center, University of Bordeaux https://orcid.org/0000-0003-0444-3098

Outi Supponen

ETH Zurich https://orcid.org/0000-0001-6738-0675

Article

Keywords:

Posted Date: July 10th, 2026

DOI: https://doi.org/10.21203/rs.3.rs-8799612/v1

License: This work is licensed under a Creative Commons Attribution 4.0 International License.
Read Full License

Additional Declarations: There is **NO** Competing Interest.

Bridging human kidney stone dynamics and damage under shock-wave lithotripsy: synchrotron X-ray imaging and tomography

Armand Sieber[‡],[1] Cameron Brewer[‡],[1,*] Bratislav Lukić,[2] Gazendra Shakya,[1] Guillaume T. Bokman,[1] Markus Belau,[3] Arvid Kühl,[3] Moritz Schlötter,[3] Kevin Schmidmayer,[4] and Outi Supponen[1,†]

[1] *Institute of Fluid Dynamics, D-MAVT, ETH Zürich, Switzerland* [‡]
[2] *European Synchrotron Radiation Facility, France*
[3] *Storz Medical AG, Switzerland*
[4] *Inria center at the university of Bordeaux, project-team CAGIRE, Université de Pau et des Pays de l'Adour, E2S UPPA, Laboratory of Mathematics and its Applications of Pau (LMAP), France*

(Dated: February 5, 2026)

Shock wave lithotripsy fragments kidney stones through transient stress waves and cavitation, yet the relative contribution of these processes in governing fracture evolution remains unclear. We combine high-speed optical imaging, X-ray phase-contrast imaging, and interleaved micro-computed tomography to resolve *in-situ* internal stone dynamics and cavitation activity alongside the three-dimensional damage progression across individual shock emissions. Clinical lithotripter shock waves are applied to two human kidney stones with distinct composition and microstructure. The measurements show that cavitation drives comminution through surface erosion and bubble collapse between internal structural layers, while fracture mechanism dominance is dictated by stone microstructure. Specifically, spallation governs ammonium acid urate failure, while calcium oxalate monohydrate ablates through cavitation-assisted delamination, despite identical loading conditions. These results clarify the respective roles of shock-induced stresses and cavitation in governing damage, providing broader insight to cavitation-mediated damage in brittle materials and a mechanistic basis for optimizing shock wave lithotripsy.

I. INTRODUCTION

Kidney stones represent hard deposits of minerals and salt forming in the urinary tract and leading to a condition known as urolithiasis [1, 2]. The prevalence of this condition exceeds 10% in certain regions of the world and has increased over the past few decades [2–4], resulting in an estimated cost of stone-related diseases over $6 billion per year by 2030 in the United States alone (adjusted to 2024 USD) [5]. Introduced in the 1980s [6], extracorporeal shock wave lithotripsy (ESWL) is a non-invasive treatment for urolithiasis that induces stone comminution through dynamic fragmentation of kidney stones by repeated generation of a focused shock wave (SW). ESWL remains more cost-effective than minimally invasive alternatives [7]. ESWL is efficient for medium-sized stones, yet produces unpredictable fragment sizes with varying kinetic energy which significantly decreases treatment efficiency in later stages [8, 9]. Nevertheless, distinct fracture mechanisms are relevant at various stages and are strongly stone-specific (*i.e.* composition, geometry, mineralogy, and microstructure). Understanding the direct physical relation of characteristics influencing fragmentation mechanisms offers a path to tailoring procedures with considerable improvement of patient safety.

Extensive work on kidney stone fragmentation has identified multiple mechanisms responsible for comminution [8, 10–15]. The physical principles governing fracture propagation within the stone include effects from the incident SW and the subsequent surrounding environmental response. Repetitive loading and unloading caused by successive SWs initiate and propagate fractures in the stone [11, 12, 14]. The incident shock induces fracture through the complex synergy of several potential mechanisms depending on stone geometry including stress gradients, tensile failure, cavitation damage, spallation, dynamic squeezing, and more. Effects driven by the response of the surrounding fluid environment, specifically with regard to cavitation, require further exploration to resolve the contribution toward efficient stone comminution.

Direct shock-stone interaction generates tensile stresses from incident, reflected, and mode converted waves that initiate and propagate fractures under repeated loading. These processes (often described within Griffith-type energetic frameworks) include tensile opening, spallation, and geometry-dependent squeezing effects to provide the baseline

* cbrewer@ethz.ch
† outis@ethz.ch
‡ These authors contributed equally to this work.

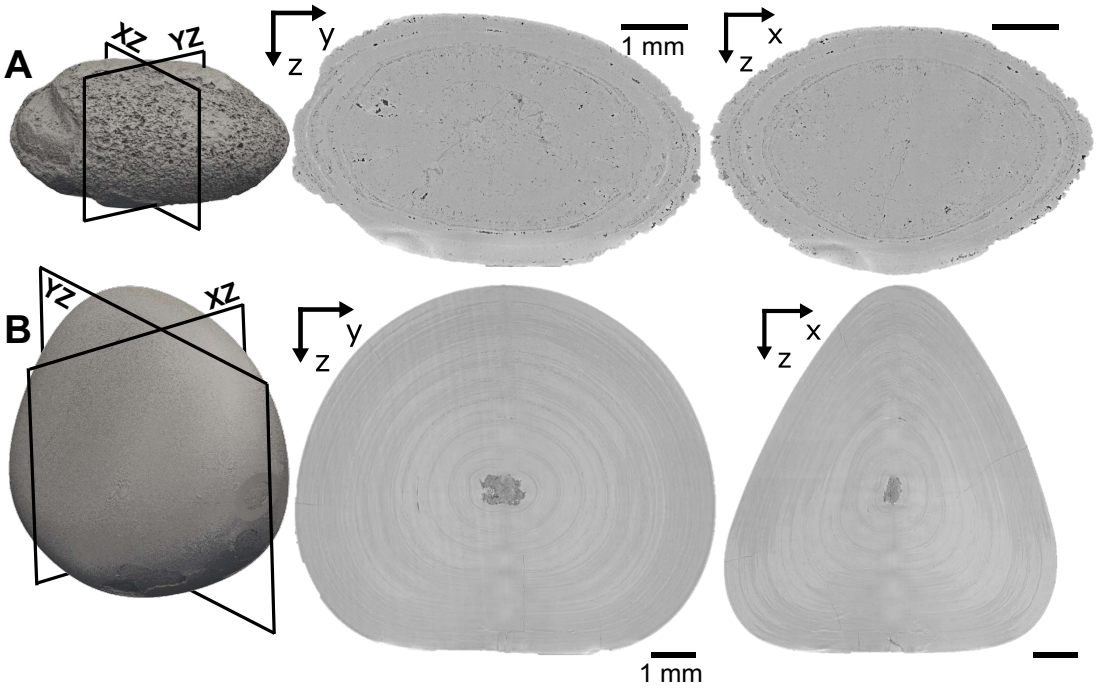


FIG. 1. The respective surface meshes and reconstructed cross-sections obtained from μ-CT of the investigated stones before treatment: (A) Ammonium acid urate (AAU) stone and (B) calcium oxalate monohydrate (COM) stone. The corresponding cross sections within the volume are identified, and scale bars are 1 mm in length relative to the corresponding cross-section.

against which cavitation-mediated damage must be interpreted [8, 10–12, 16, 17]; however, their relative influence, coupling with cavitation, and microstructure dependence remain insufficiently explored.

Although caused by SWs, cavitation (*i.e.* vapour bubble formation and collapse) offers distinct mechanisms by which damage can be inflicted upon the stone. Exposure to the tensile part of the wave leads to the formation of cavitation bubbles at the stone exterior (within the surrounding fluid environment and at the surface) [18–20], within fissures (elongated voids in the initial state), and pores (spherical shaped voids in the initial state) [21]. Upon collapse, exterior bubbles (i) form high-velocity liquid micro-jets [22–25] and (ii) emit SWs in the immediate vicinity of the bubble [26–28] capable to induce local stone stresses sufficient for surface erosion and fragmentation by serving as a focusing mechanism on the surface.

Cavitation induces erosion predominantly on the proximal surface [13, 29, 30], and the collapse of cavitation bubble clouds can produce substantial secondary SWs. High-speed optical imaging (HSOI) indicates fractures offer favourable nucleation sites and that expansion and collapse can promote fracture growth [20]. Likewise, the rebound of bubbles within confined regions of the stone interior could generate high local stress concentrations [31] leading to further fracture propagation. Since cavitation arises from the tensile part of the SW, isolating its sole contribution to fragmentation from direct shock-stone interactions remains challenging and disputed [12, 32]. Zhu *et al.* [19] suggested a coupled relationship: stress-wave-induced fractures initiate fragmentation and cavitation generates fine, passable fragments indicating internal cavitation can promote transition from separation to pulverization.

Previous 3D X-ray tomographic laboratory scale approaches enabled non-destructive assessment of internal stone damage post-mortem [30, 33, 34] suggesting composition-dependent damage patterns indicative of cavitation damage or spallation with limited resolution. Despite the significant contribution toward spatially mapping damage, the actual spatial resolution (60 μm/voxel) was unable to resolve micro-cracks necessary for accurately characterizing the damage progression towards global comminution. Only static snapshots are acquired after multiple SW exposures leaving the damage progression *per SW* undetermined and dynamic interactions incomplete. Conversely, HSOI resolves global dynamics but is limited to the stone's exterior and is obscured by the dense bubble cloud. Dynamic measurement of bubble cloud implosion has been achieved at the surface of a flat, single material plate through X-ray free electron laser imaging (XFEL) [35]. However, the direct link between the transient internal response during shock propagation and the resulting permanent internal fracture topology has remained unobserved. Resolving this relationship requires spatiotemporal coherent measurements of subsurface fracture evolution for individual SWs. Without such observations, the role of cavitation-driven mechanisms and their relationship to wave phenomenon to guide fracture

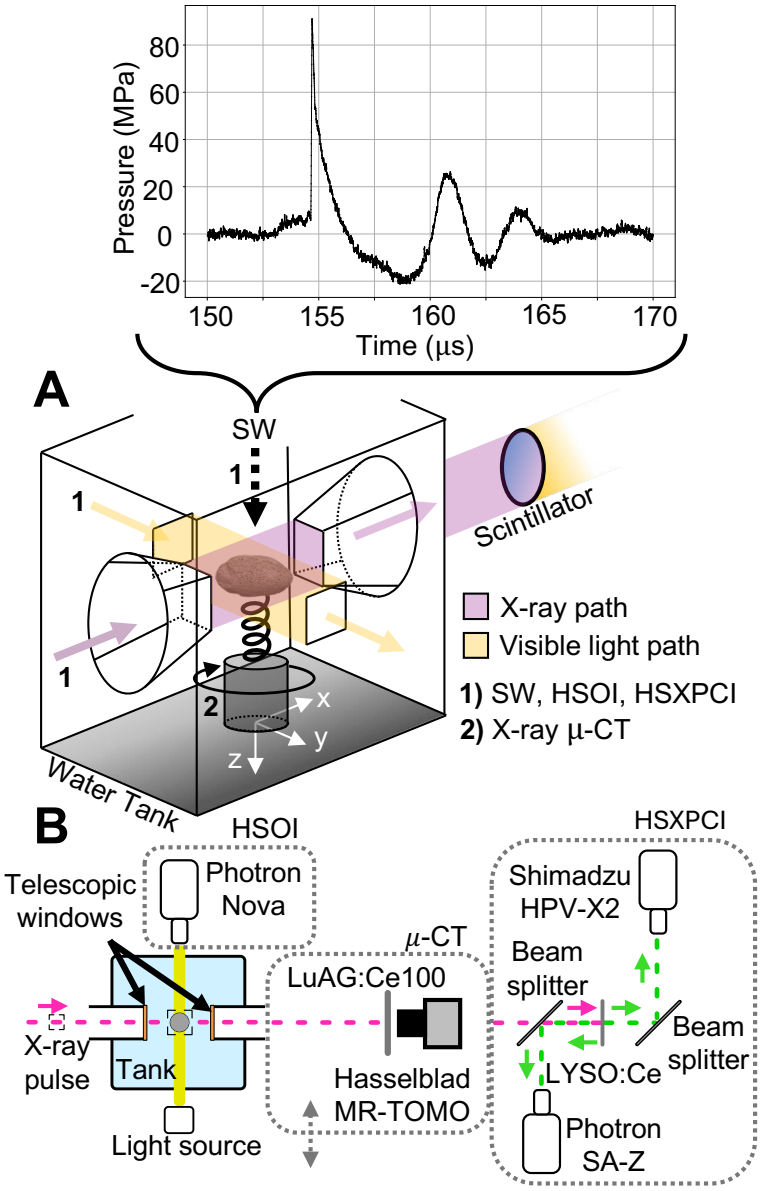


FIG. 2. (A) The experimental test chamber configuration and the pressure waveform at the focal point of the shock wave generated by the lithotripter (MODULITH® SLK ≫intellect≪ lithotripter, Storz Medical AG). The sequence of events, **1)** (high-speed optical imaging, HSOI; high-speed X-ray phase contrast imaging, HSXPCI) and **2)** (X-ray micro-computed tomography, μ-CT), is chronologically labelled and is repeated for each SW. (B) Top view of the experimental configuration is also shown.

formation are inferred rather than established, and the damage mechanisms within the specific stone microstructure remain uncertain.

In this work, three imaging modalities are combined for each SW to simultaneously achieve high spatio-temporal (100k fps and 2.27 μm/voxel) resolution, *in-situ*: HSOI, high-speed synchrotron X-ray phase-contrast imaging (HSXPCI), and synchrotron micro-computed tomography (μ-CT). The synchronized high-speed methods provide through-volume time-resolved stone response to the SW and fluid, while μ-CT performed between successive shocks provides the incurred three-dimensional (3D) micro-damage characterisation and information on damage progression stemming from the stone microstructure. Furthermore, this methodology allows direct correlation between cavitation activity and shock-induced dynamics with the resulting fracture propagation within the stone bulk, quantifying the contribution of different fracture mechanisms. Experiments were performed at the European Synchrotron Radiation Facility (ID19 Beamline) using two human kidney stones of distinct composition and microstructure: ammonium acid urate

(AAU) and calcium oxalate monohydrate (COM) (Fig. 1). The compositions were determined through X-ray powder diffraction (XRD) and results are detailed in Sec. IV. Despite exposure to identical pressure profiles (Fig. 2), the two stones visually exhibit distinct evolutions of damage (Fig. 3) governed by microstructure differences. This study establishes a *dynamic-to-permanent* correlation between cavitation driven events and internal fracture evolution in human kidney stones. These findings contribute to an in-depth understanding of the stone-specific influence on the fragmentation mechanisms and progression, which can be leveraged for patient-tailored treatments.

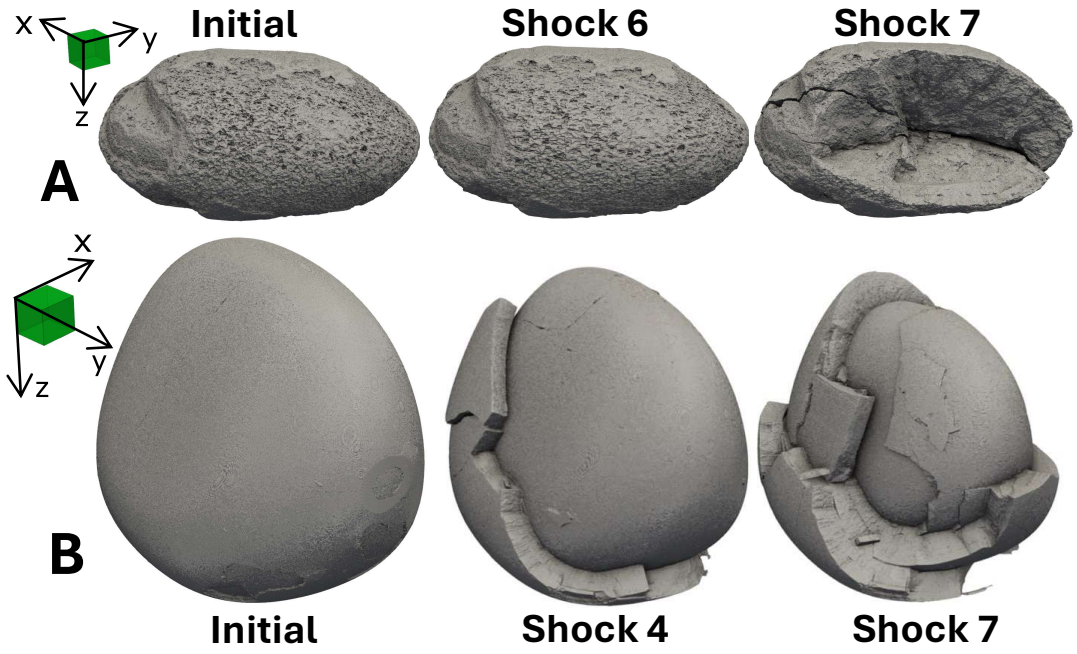


FIG. 3. The generated mesh volume from reconstructed μ-CT data shows the progressive damage after a specified number of shock waves for (A) ammonium acid urate (AAU) and (B) calcium oxalate monohydrate (COM) stones. The reference cubes possess side lengths of 0.5 mm and 1 mm, respectively.

II. RESULTS AND DISCUSSION

Optical, radiographic, and tomographic data were acquired to capture complementary aspects of the stone's response to SWL. HSOI records cavitation activity and near-surface bubble dynamics, while HSXPCI resolves the 2D projected volume-average motion and internal response. HSXPCI offers sensitivity to fringes enabling detection of fracture initiation at sub-pixel resolution, although the content within the fracture, or fissure, cannot be asserted (see Sec.IV B for further details). Between SWs, μ-CT provides a 3D map of the fracture advancement and internal morphology (Fig. 3) possessing an actual resolution of 9.08 μm/voxel. The tank configuration and experimental sequence for iterating between modalities is depicted in Fig. 2, respectively. These datasets enable correlation between dynamic loading and damage (HSOI/HSXPCI available in Supplementary Information). We present our observations in the following order: large-scale dynamic response to the cavitation and shock, identified damage mechanisms for each stone, and overall fracture progression analysis.

A. Large-scale response

The macroscopic motion of the stone under shock loading provides an initial indication of the forces acting on the stone. Synchronisation between HSOI and HSXPCI enables direct comparison and measurement of large-scale stone dynamics, cavitation, and fractures (Fig. 4).

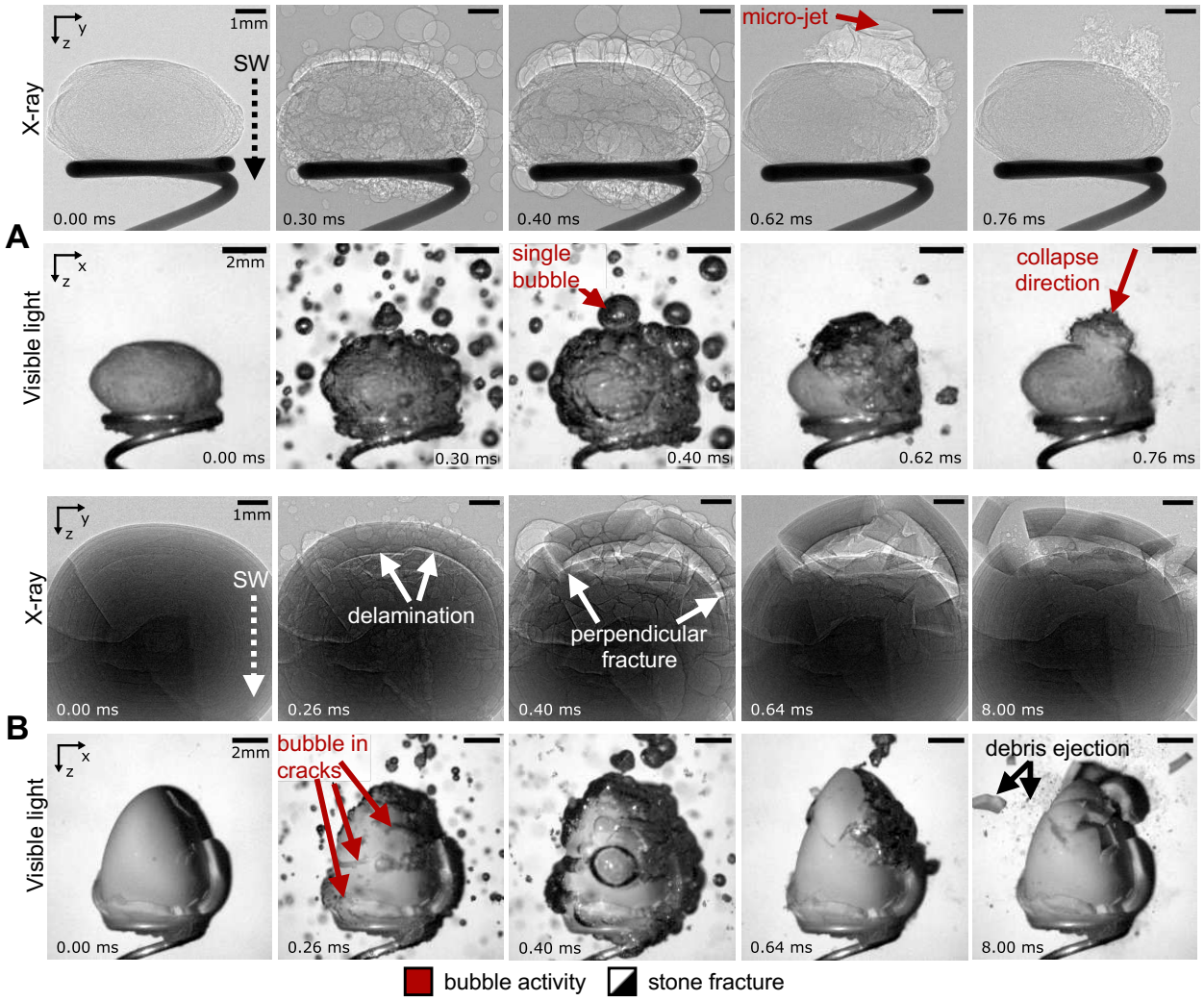


FIG. 4. Selected frames showing the dynamics resulting from the shock wave interaction with the stones. Top rows show HSXPCI frames and bottom rows show the corresponding HSOI frames. (A) Third shock on ammonium acid urate (AAU) and (B) fifth shock on the calcium oxalate monohydrate (COM) stone are depicted, respectively. The time $t = 0$ is taken as the triggering of both recordings with the shock waves reaching the stones approximately 0.25 ms later.

1. *Stone dynamic response*

Upon interaction with the incident shock, the stone experiences observable displacement resulting from the shock impulse and spring mount. For the AAU stone, the motion in the y–z plane was measured by tracking the interface between the stone and the metallic spring by an optical flow technique (see Sec. IV C). This analysis could not be performed on the larger COM stone, as the spring was out of view in the HSXPCI recording. Using displacement tracking, we extract the transient acceleration resulting from the SW and subsequent cavitation activity.

Figure 5 presents displacement, acceleration, and bubble activity for 2 ms of the AAU stone along y- and z-axes over several shocks. Cavitation activity is quantified through the surface area of bubble activity for each frame from the peripheral optical view.

Initial stone displacement from the shock occurs at 0.25 ms, reaching a maximum acceleration of 10^4 m/s^2 measured using an optical flow technique (further detailed in Sec. IV C). This is an order of magnitude lower than past assertions [32]; however, this discrepancy is resolved through the same method of analysis. Justification for the optical flow technique is provided in Sec. IV C. Following the motion resulting from momentum transfer of the shock, the stone abruptly changes trajectory at 0.65 ms corresponding to a spike in acceleration in the $-y$ and $+z$ directions. Comparison with the peripheral bubble activity profile reveals temporal coincidence with the collapse of the bubble

cloud. The temporally corresponding frame (fourth) in Fig. 4A shows a distant jet impacting the stone from the same direction triggering the hammering collapse of the surrounding cavity, confirming the acceleration spike corresponds to bubble cavitation collapse.

The sharp transient acceleration from cavitation is roughly double the acceleration resulting from the SW (in the z-direction) which implies a significant cavitation-induced impact on the stone surface at this instant. However, precise quantification of the force remains limited by several factors: (i) displacement was captured only in one plane (preventing an x-axis component); (ii) rotational motion is not resolved; (iii) the measured response does not decouple the spring and SW influence.

To better interpret the dynamics from a clinical perspective, it is relevant to compare the effective stiffness of the spring mount to kidney tissue. Using nano-indentation, the effective elastic modulus of kidney tissue has been probed to an average of 3.84 kPa [36]. Differentiating the Hertzian law for spherical indentation [37], the effective Young's modulus, E^*, can be translated to a stiffness constant, k, through the equation

$$k = 2E^* R^{1/2} h^{1/2}, \tag{1}$$

where R is the probe radius and h is the indention depth. Based on the parameters of the referenced study [36], we calculate the stiffness of the tissue as 0.15 N/m, which is several orders of magnitude lower than that of the compression spring used in this experiment (1140 N/m). Therefore, the designed system experiences a smaller dynamic response than exists *in vivo*. This discrepancy likely does not alter the mechanisms identified, but indicates the translational and rotational dynamics presently observed underestimate motion expected *in vivo*. We emphasise the need to account for tissue compliance when translating these results to clinical settings.

2. Cavitation activity

Numerous cavitation bubbles nucleate within the surrounding liquid and on the stone surface. In the AAU stone, bubbles rapidly envelop the surface (Fig. 4A). The COM stone exhibits similar behaviour during initial shocks, yet bubbles increasingly nucleate along emerging fracture lines and discontinuities resulting from the delamination of outer layers (discussed further in Sec. II C 1). These regions are highlighted in Fig. 4B (frame two).

The bubbles merge into a dense cluster which gradually covers large regions of the COM stone and entirely envelops the AAU stone. This greater surface coverage for the AAU stone results from the favourable nucleation sites provided by its rough surface (specifically compared to the smooth exterior of the COM stone). Additionally, the central cross-section in the x–y plane of the AAU stone is roughly 90% of the lithotripter focal cross-sectional area. The small size of the stone relative to the 6.3 mm focal width of the SW exposes it to a more uniform negative pressure field. Following maximum expansion, the bubble cluster collapses asymmetrically toward the proximal stone surface and subsequently rebounds. On the AAU stone, the collapse consistently occurs in the upper-right region (on y–z plane), as visible in frames four and five of Fig. 4, suggesting a stable cavitation focus and leading to local erosion (discussed further in Sec. II B 2) consistent with implications of past work [20, 30]. The bubble cloud creates multiple layers of cavitation that encompass the upper part of the AAU stone leading to cascading collapse. The outer layer of single bubbles collapse first, focusing the energy to the dense inner layer collapse (compare frames 3 and 4 in Fig. 4A) directing energy inward toward a surface point. It seems likely from the localised asymmetrical cloud collapse consistency of the surface cavity that this phenomenon is coupled with the jetting of the distant bubble (see Fig. 4A, frame 4 and 5) [38].

Comparable dynamics are observed for the COM stone. Nevertheless, it undergoes steady material loss for each SW, resulting in fewer exterior nucleation sites. Cavitation bubbles nucleate and collapse preferentially along surface fractures and discontinuities (arrows in Fig. 4B) prior to lamellae detachment. This behaviour aligns with observations by Pishchalnikov *et al.* [20], who identified localised bubble collapse as a key fragmentation driver, and by Field [31], who proposed that bubble rebound within confined geometries promotes fracture propagation. We observe a similar process: bubbles expanding from fracture edges appear to lift and separate thin lamellae (see Fig. 4B frame two) which can directly contribute to the delamination of the stone surface.

B. AAU damage mechanisms

The AAU stone exhibits two concurrent forms of damage during SWL: (i) internal fracture driven by spallation and (ii) localised surface erosion from cavitation activity.

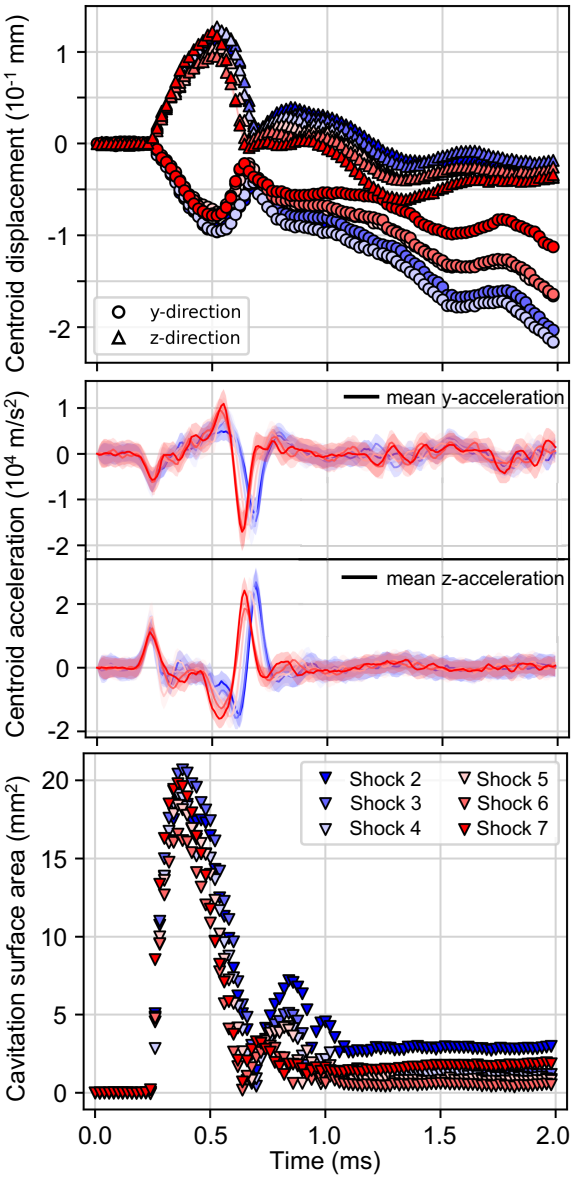


FIG. 5. Displacement of the stone along y- and z-directions (top) relative to X-ray coordinate system extracted from the high-speed recording, the associated accelerations (middle), and the peripheral cavitation activity (bottom) are plotted for multiple SWs of the AAU stone. The time $t = 0$ triggers both recordings with the shock waves reaching the stones approximately 0.25 ms later. Residual cavitation activity measured beyond $\sim$ 1.0 ms is due to erroneous classification of ejected debris and dust as cavitation in the images.

1. *Spallation*

Development of an internal fracture is identified in Fig. 6 culminating in fragmentation after seven SWs. The measured spallation focal region aligns closely with simplistic predictions for spallation failure locations [39, 40] at the characteristic distance $l = \frac{ct}{2}$ where c is the longitudinal wave speed and t is the pulse duration (assuming an ideal rectangular wave and ignoring material strength). For uric-acid stones with wave speeds of 2800–4550 m/s [41] and pulse of 1 μs, this yields a theoretical spallation range of 1.4–2.28 mm from the distal surface (highlighted red in Fig. 6A). Our central spallation region, 1.92 mm from the distal surface, is within this interval suggesting spallation is the primary fragmentation mechanism for AAU. The focal region is identified by the intersection of three major fractures (Fig. 6A).

The development of the individual central damage feature is rendered spatially within the stone (Fig. 6B) demon-

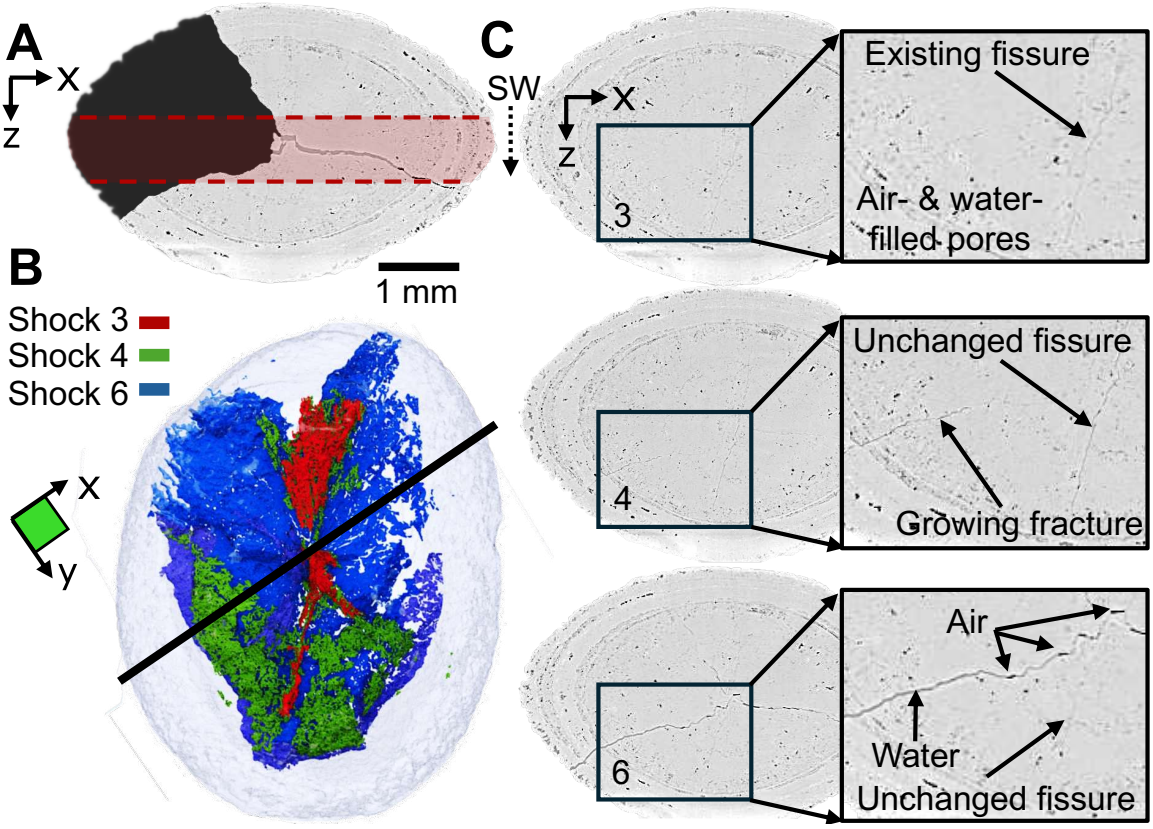


FIG. 6. The reconstructed cross-sections from μ-CT through the x–z plane are depicted for the final fragmented stone (A) and for shocks 3, 4, and 6 (C) showing the damage evolution and material phases of stone (light grey), water (dark grey), and air (black). (A) The silhouette of the initial stone boundary shows the material loss after the final SW, and upper and lower bounds depict the estimated region of spallation calculated from the longitudinal wave speed of the material. (B) The growth of the prominent fracture resulting from spallation is depicted spatially within the AAU stone from a top view (x–y). The representative cube is 0.5 mm in length. (C) The presence of existing fissures and developing fractures are identified for the same cross-section across multiple SWs.

strating that spallation fractures expand from the centre and coalesce with neighbouring voids. A thin fracture appearing to initiate within the porous network between SW 3 and 4 is indicated in Fig. 6C which merges with the central spallation fracture in the sixth shock. Entrapped air and water from the porous region remain within the fracture offering favourable heterogeneous cavitation nucleation sites thereby generating pressure on the fracture walls. Noticeably, the sixth SW causes significant damage as fractures reach the stone exterior (see also Fig. 10) prior to failure. Supplementary Video 2 highlights bubble growth from interior spall fractures. Although cavitation activity within voids (porous regions and growing fractures) may contribute to local opening or fracture, the effect cannot be conclusively decoupled from tensile stresses associated with spallation in this experiment.

However, we assert that the propagation of the spallation induced fracture is strongly governed by the distribution of these mixed-fluid regions. The fracture preferentially advanced through porous regions while leaving prominent neighbouring existing fissures unaffected for all SWs (enlarged in Fig. 6C). These saturated existing defects, though serving as natural stress concentrators, do not open further suggesting that the presence of entrapped air, rather than geometry alone, facilitates the repeated opening and closing cycles driving spallation fracture progression. Similar internal air pockets have been reported in *ex-vivo* stones and suggested within *in-vivo* stones indicating the pore-driven fracture pathway offers clinical relevance [42, 43].

2. *Surface erosion*

Measuring surface erosion requires a stable exterior boundary over multiple shocks. Because COM ejected lamellae after nearly every SW, a consistent surface feature could not be determined. Therefore, erosion analysis was performed only for the AAU stone, and restricted to the upper region (see Methods Sec. IV C).
Orthogonal arrangement of the high-speed visible-light and X-ray cameras (Fig. 2B) enabled identification of the collapse location of the cavitation bubble cloud. This collapse surface point remained highly consistent across shocks and exhibits the largest measured surface erosion. After four shocks, the tomographic surface difference maps (from point-cloud analysis in Sec. IV C) indicate minimal erosion, yet high-speed imaging records a fine dust cloud ejected from the surface during early shocks (Fig. 7). A more substantial surface change occurs after the fifth shock. Large debris fragments detach from the same localised region (captured by HSOI in Fig. 7). The surface map after the sixth shock captures the most pronounced erosion pattern at the cavitation cloud collapse site.
Our synchronised HSOI and HSXPCI visualise the moment and location where the impinging jet initiates asymmetrical bubble cloud collapse, striking the stone with a hammering effect (Fig. 4A). The generation of dust and debris (Fig. 7) supports past work asserting cavitation serves exactly this role [19]. The cascading behaviour of the collapse, for the AAU stone particularly, has already been discussed (Sec. II A 2), yet we emphasise the capability of bubbles at the outer layer to contribute to the load of the collapse.
Although cavitation-induced surface damage appears to constitute a minor fraction of the overall damage for AAU, we highlight the stone fragments in only seven shocks. For clinical scenarios (often involving hundreds to thousands of shocks), erosion may pose larger significance. Moreover, erosion sites themselves may act as nuclei for future fracture initiation, as pits or weakened regions from jet impact can concentrate stress during subsequent loading.
The strong spatial correlation between the jet impact and subsequent bubble cloud collapse location, combined with the measured erosion map, captures the complementary nature of the discussed mechanisms. Spallation dominates fracture propagation, while cavitation collapse governs material removal in a spatio-temporally repeatable manner.

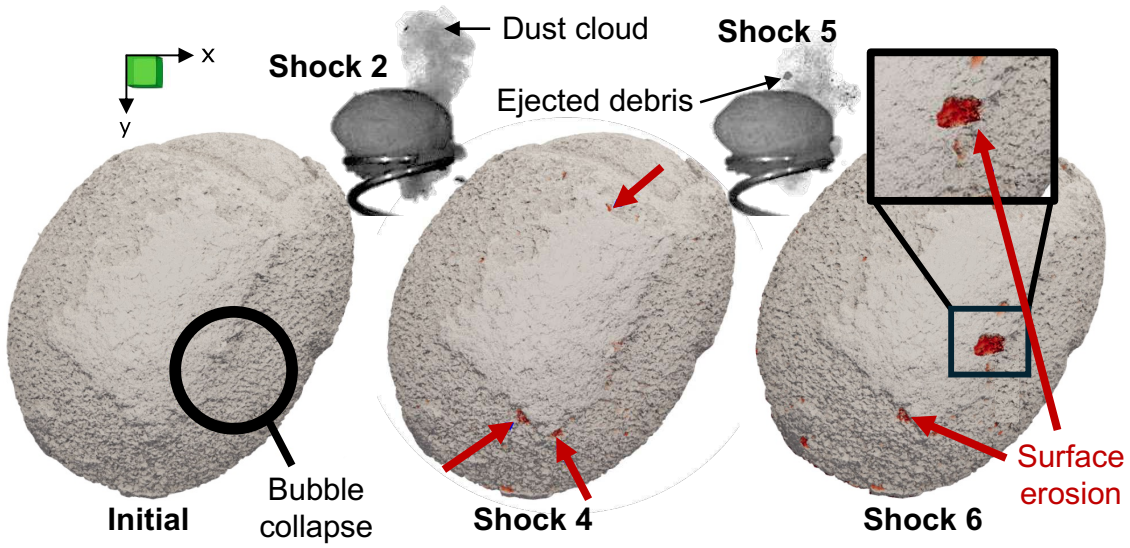


FIG. 7. Volume rendering of the AAU stone (generated from μ-CT data) at various stages, showing the emergence of erosion patterns on its upper half, with snapshots capturing dust clouds and debris ejected 1.75 ms after the shock wave impact. The red arrows highlight the locations of erosion, and the representative cube has a length of 0.5 mm.

C. COM damage mechanisms

Resulting from a layered microstructure, damage evolution in the COM stone differs fundamentally from the spallation-dominated response observed in the AAU stone. Cavitation offers a strong contribution toward fragmentation, not only as an exterior mechanism, but inside fractures. As material of the outer layer is ejected, the geometry and stress distribution in remaining layers evolve dynamically, giving rise to fracture modes deviating from the plane of delamination.

1. Delamination

Delamination is the primary mechanism responsible for material ablation in the COM stone, arising directly from its composite and radially organised microstructure. Fractures consistently initiate along interfaces between layers, and therefore, tangential to the surface (Fig. 4B and Fig. 8). This behaviour mirrors predictions of Cleveland and Tello [44], who numerically demonstrate that composite stones redistribute the peak negative pressure generated during the tensile part of the shock toward the layer interface. This shift increases fracture likelihood along that boundary, rather than within the dense stone layer.

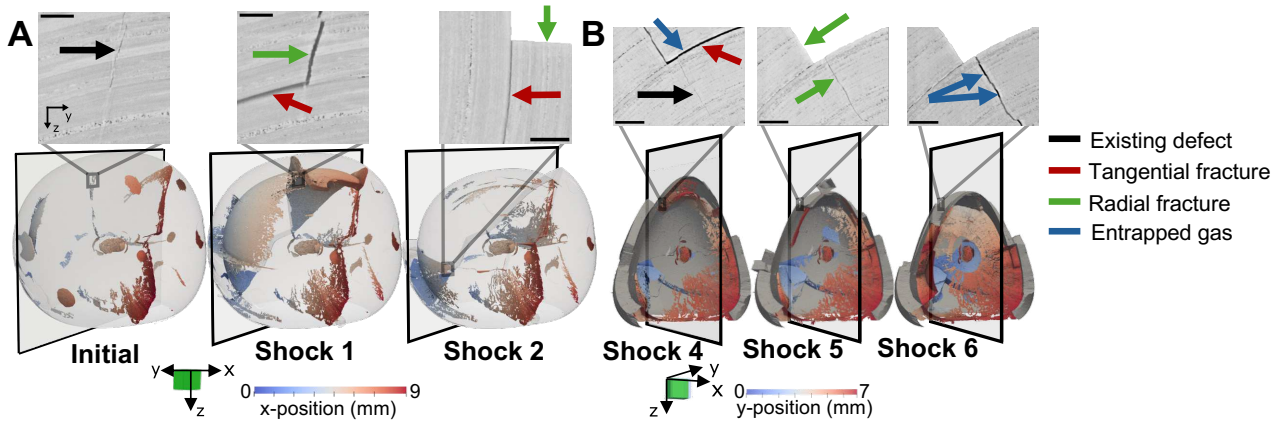


FIG. 8. Enlarged portions of tomograph slices (top) and volume renderings (bottom) from μ-CT of the COM stone at different stages are shown, illustrating the development of a fracture parallel to the stone surface and its gradual delamination. The volumes are displayed as surface meshes (representative cube length of 1 mm), with the stone's exterior highlighted in a semi-transparent overlay and its large internal voids rendered in a blue-to-red colour gradient proportional to the voxels' position, x- and y-axis respectively for (A) and (B). Small internal voids are excluded from visualisation. The figure is rotated to highlight internal regions relevant for discussion.

Likewise, we observe the first delamination event originates from an existing fissure radial to the surface near the proximal end of the stone ("initial" frame in Fig. 8), indicating that the composite structure strongly governs concentration of stresses. Once initiated, the fracture rapidly advances along the tangential direction, producing partial separation of the outer layer. Although insufficiently fast to resolve the crack tip speed, HSXPCI (Fig. 4B) reveals the opening of these interlayer fractures during the tensile portion of each SW. The strong tensile part causes rapid bubble expansion within fissures possessing air and water suggesting contribution toward delamination.

Cavitation activity contributes not only to ejection of external lamellae from the outer layer (Fig. 4B) but also appears capable of mobilising internal layers. Figure 9C depicts a tomograph at a consistent location in the stone (measured from the distal end) across multiple shocks illustrating both the evolving entrapped gas distribution and the displacement of internal structures. Corresponding HSXPCI frames in Fig. 9A–B show the stone during the maximum compression and tension part of the incident SW. Across successive shocks, the interior core (indicated in Fig. 9) undergoes upward translation, while the surrounding outer layer primarily expands laterally. Notably, the core continues to translate upward despite the weight of a comparatively large outer layer above (at the time of SW 9 and 10). This behaviour indicates the interior core is mechanically disconnected from base material, allowing independent response to the cavitation of entrapped gas below. The simultaneous cavitation activity and upward displacement of the interior core suggests the bubble expansion generates forces sufficient to lift the core and upper layer. This observation reinforces assertions from Ren *et al.* regarding object displacement from cavitation [45]. By measuring centroid displacement during the tenth SW over a 12.8 ms interval, the mean velocity of the ejected upper layer is estimated at 0.158 m/s in the y-z plane. The z-component alone is 0.152 m/s meaning the overall displacement is primarily upward.

The bubble collapse between the interior core and base layer generates fragments spanning micrometres to millimetres in length, as labelled in Fig. 9. The production of fine debris (HSOI frame five of Fig. 4B) and micro-scale fragments (Fig. 9) at the site of bubble collapse between upper and lower delaminated layers, respectively, demonstrates the critical role of cavitation to produce passable fragments [19] for the COM stone microstructure. However, the mounted spring stiffness in this experiment (relative to renal tissue) likely amplifies the impact between layers for the COM stone promoting micro-scale fragment production.

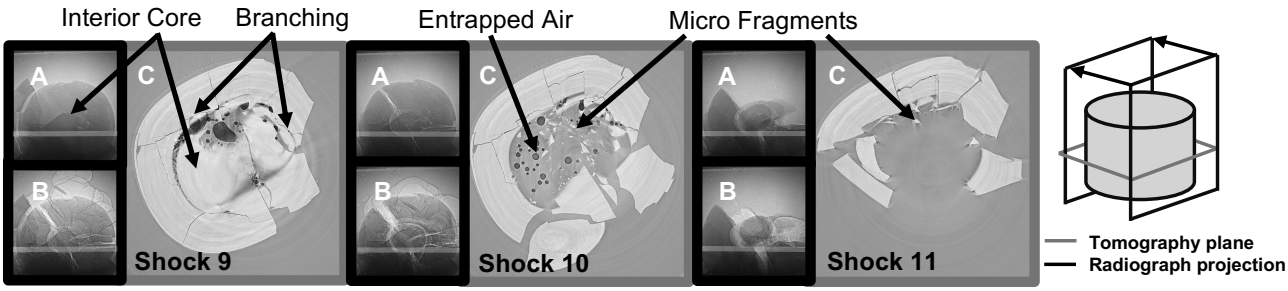


FIG. 9. Entrapped gases are shown expanding and opening fractures during the tensile part of the incident wave and the ability of entrapped air to contribute to material ejection is shown. High-speed X-ray projections (from HSXPCI) show (A) the compressive part of each shock and (B) the moment of maximum separation within the fractures, while (C) CT from the same plane for each shock shows entrapped air within stone crevices contributing toward the ejection of material.

2. Fracture deviations

As delamination progresses, the tangential-propagating fractures between two stone layers often lead to fracture advancement in an outward normal direction to the surface (radial-propagation fractures). These features are identified in the tomographs of Fig. 8A and rendered within the stone volume. The transition from tangential (layer-parallel) to radial (outward normal) fracture propagation reflects a shift in the local stresses expected in the brittle outer layer due to bending action. As the exterior layer dynamically deforms from the outward radial pressure (from cavitation and SW reflections), outward normal fractures are initiated from the tension generated from circumferential stresses within the outer layer inner radius. However, beyond the fourth SW, these fractures penetrate deep into the stone, evident from internal void volumes rendered in Fig. 8B depicting fracture advancement toward the stone centre. The most likely explanation is fissures below the spatial resolution cause deviation of the propagating tangential fracture toward the direction of the fissure. Such discontinuities can arise from crystal formation [46]. As opposed to the unaffected saturated fissures in the AAU stone (Sec. II B 1), air-filled tangential-propagating fractures entrap air within the fissure creating a heterogeneous bubble nucleation site for subsequent SWs. This phenomenon is identified in Fig. 8B. Divergence from the tangential-propagation could also be caused by a high density inclusion within the stone. A high density discontinuity corresponds to a localised increase in greyscale within the volume. Because no visible high density feature is detected, this is an unlikely explanation for the current case, yet could play a role in other stones. A further cause promoting deflection of fracture growth is the fracture-tip speed. Dynamic fracture growth approaching or exceeding the Rayleigh wave speed limit may induce fracture-tip instability resulting in sudden propagation deviations.

In addition to the radial-propagating fractures (both oriented away from and toward the stone centre), branching of fractures occurs at the base of the stone. In Sec. II C 1, we emphasise the impact between two layers initiating debris and micrometre ejection. In Fig. 9, thin fractures are visualised branching throughout the base layer where this inter-layer impact is occurring. The spring likely amplifies the impact in comparison to *in-vivo* SWL, yet over hundreds of repeated compressions and releases, growth of small imperfections can result in similar branching fractures [47].

D. Stone damage quantification

Measuring the damage progression within both stones required a segmentation strategy capable of resolving interior and exterior geometric changes with high fidelity at each SW. Tomographs were processed in three stages: (i) foreground isolation, (ii) solid-fluid phase classification, and (iii) air-water classification. Section IV C details the semantic segmentation method. From the labelled dataset, the internal and external surface areas were computed independently for every SW (excluding the first AAU SW, which drifted). All percent-change values are referenced to the initial surface area, enabling cumulative damage measurement throughout treatment. Measuring the surface area change, as opposed to volume change, prioritises fracture growth over mass loss in the analysis. Despite initial minor overall increases in surface area after two SWs, the AAU stone exhibits a stable internal and external surface area for the subsequent two SWs (SW 3 and 4 in Fig. 10). At this stage, fractures growing within the air- and

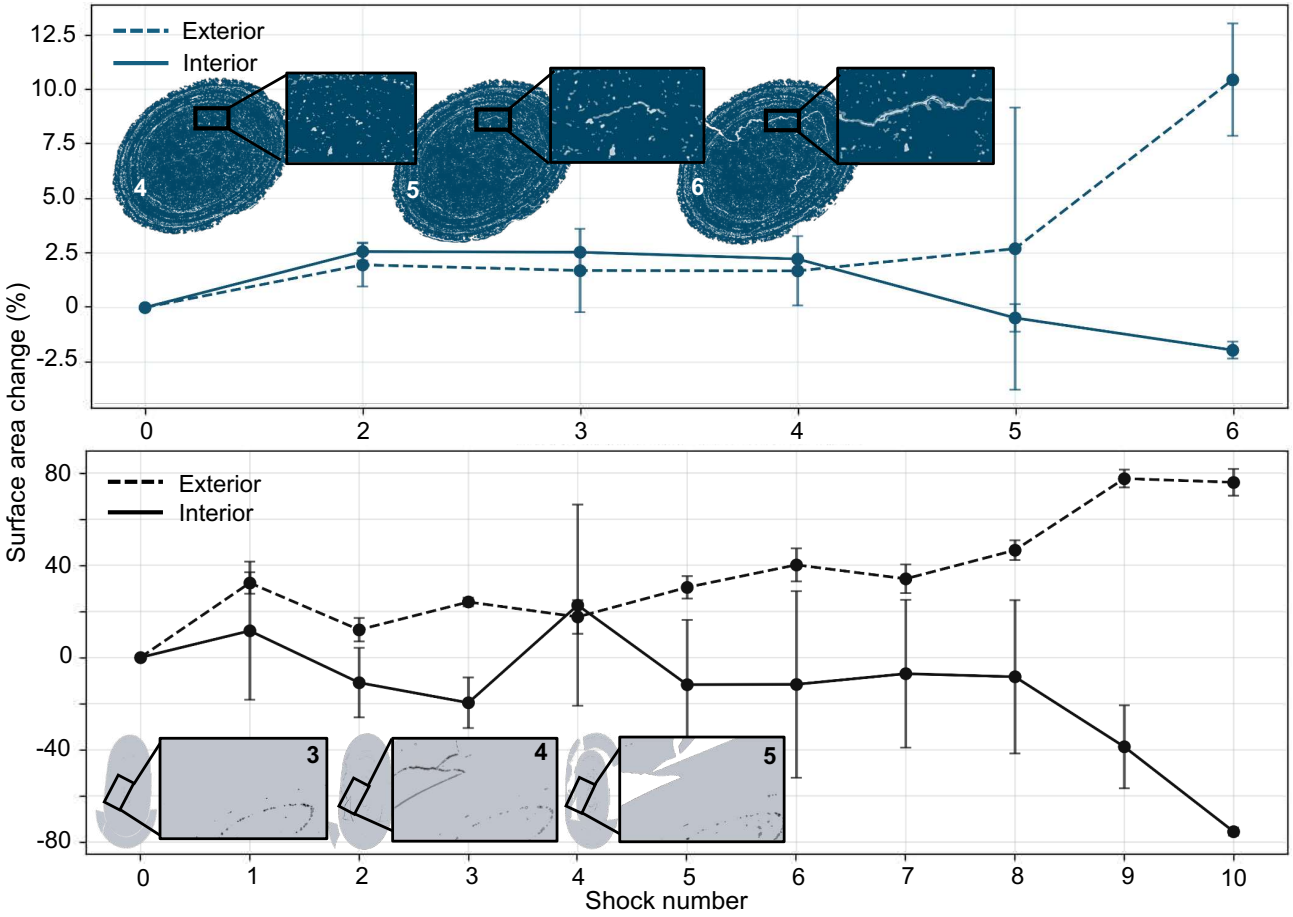


FIG. 10. The percent change in the internal and external surface area of the AAU (top) and COM (bottom) stone is quantified and plotted per shock. The same labelled tomograph is depicted across three shocks to demonstrate the physical representation of this profile within the stone.

water-mixed porous region remain largely isolated from the central spallation region (enlarged representations in Fig. 10 and Fig. 6C). Both remain within approximately +2.5% from the baseline over first several shocks, consistent with the slow, centrally governed fracture propagation described in Sec. II B 1. Upon the fifth SW, fractures begin to penetrate the porous network (see segmented tomographs in Fig. 10) and extend to the stone exterior on the sixth shock. This observation is measured as an exterior surface area increase of roughly +12.5%, consistent with the large fracture rendered in Fig. 6B. Once entrapped air within the porous region interconnects with the central spallation region, failure is induced within 2–3 SWs.

The relatively small magnitude of the internal percent surface area change is attributable to the porous microstructure. Because AAU initially possesses a comparatively large internal surface area, additional fractures represent only a marginal increase until approaching the external boundary. The AAU fracture evolution is dominated by a centrally initiated wave phenomenon and propagation is enhanced by the presence of interconnectivity to entrapped air leading to eventual fragmentation.

Contrastingly, the surface area profile of COM has a large range, reflecting the continual delamination and rapid generation and removal of thin interior fracture structures from the first shock onward. Internal change in surface area oscillates sharply: −20% (third), +20% (fourth), −10% (fifth). These variations correspond to fine-scale interior fractures developing within the stone, yet quickly exposed to the exterior after a single shock interval (Fig. 10). Once exposed, these structures no longer contribute to internal surface area, represented in large profile swings seen between SW three–five. Ultimately, the COM stone reaches a change of nearly −80%. The stone has little internal surface area initially, so each inclusion or void exposed results is a disproportionately large fractional decrease. Therefore, this magnitude of negative change is expected.

Exterior surface area steadily increases throughout treatment related to persistent delamination (Sec. II C 1). One may expect even larger external percent increases; however, most delaminated material was ejected and therefore absent for subsequent CT scans. Large uncertainty for the COM internal surface area measurement arises from thin

branching fractures (see Sec. II C 1, Fig. 9, and Fig. 10). However, it is clear the overall trend is consistent and physically represented by features within the stone. Elaboration upon segmentation uncertainty quantification can be found in Sec. IV C.

III. CONCLUSION

This work demonstrates a novel experimental method for directly connecting high-speed cavitation dynamics with internal damage incurred by kidney stones and is demonstrated for two kidney stones with distinct composition and microstructure. Combining high-speed optical imaging (HSOI), X-ray phase-contrast imaging (HSXPCI) and micro-computed tomography (μ-CT), we observe, not only the stone dynamic response and cavitation activity, but also measure the corresponding internal fracture progression for each shock-wave (SW). This approach enables mapping specific fracture modes to the microstructure features which promote them.

The stones (ammonium acid urate, AAU; calcium oxalate monohydrate, COM) exhibit distinct fragmentation mechanisms, emphasising kidney stones of differing composition and microstructure do not respond uniformly to identical SWs. In the AAU stone, spallation initiates fractures rapidly and results in full fragmentation within 2–3 SWs once the central spallation region possesses connectivity to the porous air- and water-mixed region. Concurrently, surface erosion occurs through the impact of cavitation jetting and cloud collapse. For clinical situations, the number of SWs required to fragment the stone is often orders of magnitude larger than required in this study potentially arising from attenuation and dephasing in the body. However, by obtaining the stone shape prior to SWL, we posit that optimising the treatment orientation which maximises the focal amplification from the quasi-ellipsoidal distal surface can lead to efficient stone comminution in future treatments. Additionally, our assertion regarding internal connectivity between fractures initiated in the spallation focal region and porous region offers relevance to clinical treatment because of the presence of entrapped air within kidney stones *in-vivo* [42, 43].

Conversely, the layered structure of the COM stone promotes delamination ablation, where fractures propagate tangential to the surface and experience secondary deviating fractures resulting from delamination. The ejection speed of a layer fragment is estimated and offers relevance to patient safety during treatment. We expect generation of less micro-fragments at the stone base *in-vivo* compared to the present study resulting from the stiffness discrepancy between renal tissue and the spring mount. However, fatigue experienced during repeated loading in clinical settings will likely promote further branching fractures than identified presently.

Despite the difference between the two stones, both generate multiple length scales of fragments including passable debris resulting from cavitation collapse either at the stone surface or between stone layers, emphasising cavitation as an effective mechanism for comminution.

Cavitation activity consistently displaces stones, opens fractures, and produces measurable surface erosion. While erosion remained minor over the limited number of shocks, HSXPCI clearly indicates cavitation can dislodge both external and internal layers. However, cavitation and shock-induced stresses could not be completely decoupled in this study. Future experiments must independently quantify the respective contribution of each in fracture propagation and fracture initiation.

The present study demonstrates HSXPCI interleaved with micro-computed tomography provides a unique capability to determine *when* specific fracture mechanisms dominate with regard to the sequence of SWs, dynamic stone behaviour within a specific shock event, and spatially resolve fractures corresponding to the stone microstructure for each SW. By examining the two compositionally distinct stones, we show this framework is robust for markedly different material structures and can resolve rapid transitions between mechanisms as conditions evolve. The resulting datasets serve as a benchmark for interpreting how microstructure, entrapped gas and liquid, and local stress evolution guide fracture trajectories. Extending this approach to additional clinically relevant compositions and to synthetic analogues will help isolate governing physical features and reduce the complexity inherent in natural stones. Such expansion will not only clarify how fracture mechanisms initiate, interact, and exchange dominance during SWs, but will also establish a comprehensive experimental database upon which advanced multi-physics models can be built. Collectively, these advances provide a path toward mechanistically informed optimisation of shock wave lithotripsy.

IV. MATERIALS AND METHODS

A. Stone composition and prevalence

Two human kidney stones were investigated, each composed predominantly of a single mineral phase: ammonium acid urate (AAU) and calcium oxalate monohydrate (COM), respectively. For context regarding the prevalence of

these stones, calcium oxalate is the most prevalent mineral in kidney stones for both men (81.7%) and women (68.6 %) [48]. In contrast, AAU stones are rare in high-income countries, appearing in less than 1% of cases, though their prevalence can be higher in specific regions [49]. X-ray powder diffraction was used to determine the composition. By comparing the measured diffraction intensity profile to characteristic peaks (or *fingerprint*) for a database of minerals, we determined the most likely composition within the stone and concluded that the AAU stone possesses traces of calcium oxalate. The analysis was performed using a powder X-ray diffractometer (Empyrean 3, Malvern Panalytical). Correspondence between the diffraction intensity profile and asserted material fingerprint can be found in Supplementary Information 1. As a result of the respective compositions, the internal stone microstructures differ substantially.

Visualisation of the two stones is provided in Fig. 1, showing both reconstructed surface volumes and representative tomographic slices. The AAU stone measures $5.8 \times 6.2 \times 3.8$ mm^3 with a porous and overall homogenous interior structure. The porous interior is largely unordered and is encapsulated within a thin, rough outer surface. Existing fissures are evident prior to treatment. Through tomographic segmentation (further details in Sec.IV C), we estimate the interior porosity to be roughly 2.5% void fraction.

In comparison, the COM stone measures $7.5 \times 9.5 \times 8.3$ mm^3 and displays a laminated interior structure. A central core, encircled by thin, radially growing lamellae, result in a smooth outer surface. This stone also exhibits internal fractures prior to treatment both tangential to its surface and in the radial direction. Segmentation of this stone indicates the void fraction porosity to be approximately 0.12%.

The two kidney stones were fully immersed in water prior to experimentation (30 and 56 hours for the AAU and COM stone, respectively). The samples were received from a medical doctor; however, their extraction method and prior clinical history are unknown.

B. Experimental details

Experimental setup

The shock waves were generated using a medical-grade electromagnetic lithotripter (MODULITH® SLK ≫intelect≪, Storz Medical AG) capable of producing peak positive pressures up to 91 MPa. The dynamic response of each stone at the moment of shock-stone interaction was captured *in situ* by synchronising high-speed X-ray phase contrast imaging (HSXPCI) and high-speed optical imaging (HSOI) at two different frame rates. Between successive shocks, once motion within the chamber ceased, phase-contrast μ-CT scans were acquired to resolve the subsurface, 3D evolution of internal fracture networks. A schematic of the experimental configuration and test chamber are provided in Fig. 2. The stones were positioned at the lithotripter focus inside a transparent $100 \times 100 \times 100$ mm^3 test chamber, filled with deionised and degassed water. Oxygen gas content was measured to be 2.22 and 2.60 mg/L O_2 for the AAU and COM stone, respectively. The chamber is equipped with telescopic windows of Kapton® polyimide film designed to minimise X-ray beam absorption and avoid confinement effects associated with the boundary influence on the shock wave [50]. Stone alignment with the lithotripter focus was performed using an integrated ultrasound targeting system.

To mount the stones with minimal mechanical interference, each specimen was glued to the end of a compression spring with 5.5 mm outer diameter, 0.5 mm coil diameter, and stiffness $k = 1.14$ N/mm. This mount allows for translation motion induced by the shock-stone interaction and cavitation impact while maintaining sufficient rigidity to ensure stationary consistency during μ-CT (ensuring sharp boundaries and minimising drift artifacts).

High-speed imaging

Experiments were performed at the European Synchrotron Radiation Facility (The ID19 Beamline), operating in 16-bunch mode (75 mA). This mode provides a continuous train of $\sim$ 100 ps X-ray pulses at 176 ns intervals. The long distance between the source and sample (145 m) along with the small source size (less than 0.1 mm) yields a highly coherent beam suitable for phase-contrast imaging.

X-rays transmitted through the stone were converted to visible light by an LYSO:Ce scintillator and recorded using a Shimadzu HPV-X2 (880 ns interframe time with spatial resolution 30.9 μm/pixel) and Photron SA-Z (10 μs interframe time with spatial resolution 19.2 μm/pixel). Simultaneous shadowgraphy was performed using a Photron Fastcam Nova S12 (20 μs interframe time with spatial resolution 57.3 μm/pixel) providing complementary optical views of cavitation activity and large-scale stone motion.

Micro-computed Tomography

Full 360-degree tomography was performed on the sample with 75 keV beam energy and 0.01 s exposure time. The poly-chromatic X-ray beam from the Wiggler source is converted to visible light by a LuAG:Ce100 scintillator source, at which point the projection can be absorbed by the Hasselblad camera sensor. Half-acquisition (offset centre of rotation) maximised the field of reconstruction while maintaining the 2.27 μm voxel resolution. The spatial domain was reconstructed from phase-contrast X-ray projections, and the optimal δ/β value for Paganin method filtered back

projection was determined to be 150. Through phase-contrast imaging, edges can be resolved at 10% of the length of a single pixel; however, to effectively evaluate the interior greyscale of a region requires resolution of 4 pixels (or voxels) in breadth.

C. Data Processing

Optic flow technique

The displacement of the stone over time (for the AAU stone) in the y–z plane was determined for HSXPCI through Lucas-Kanade optical flow algorithm implementation in OpenCV. Motion detection in the x–y plane was not feasible due to cavitation activity obscuring the stone using visible light imaging. This implementation assumes the glued spring and the stone rigid body motion are identical. The contrast between the dense metallic spring and surrounding water offered a stable and distinct object suitable for optical flow tracking.

Twelve user-identified points along the edge of the spring-stone interface were used to initialise particle tracking between frames and to compute a centroid for tracking rigid-body motion. The forward-backward tracking inconsistency was measured to be less than 0.1 pixels. From the centroid trajectory, translation along two axes and a rotational component (not used in this analysis) were obtained. Acceleration was estimated by fitting a smoothing spline to the position data and computing the second derivative of the resulting piecewise spline (less sensitive to noise than raw position measurements). The spline fitting was performed using a Python implementation of Woltring's gcvspl Fortran algorithm [51]. Manual tuning is not needed because the smoothing penalty is selected through generalised cross-validation. Alternative differentiation methods, such as the Savitzky-Golay filter, were also evaluated and yielded similar results. Uncertainty in the acceleration arising from centroid localisation error was quantified from Monte Carlo simulation. Ten thousand trajectories were generated by introducing Gaussian noise perturbations ($\sigma = \pm 0.25$ px, an upper bound given the forward/backward inconsistency) to the centroid position at each time. The resulting acceleration ensemble was used to compute the mean acceleration, which is presented with a unit standard deviation in Fig. 5.

We note our acceleration estimate is an order of magnitude lower than the range estimated by Wess and Mayer, despite nearly identical pressure profiles (90 MPa peak positive pressure and 1 μs duration) [32]. Their estimate (10^5 to 2×10^5 m/s^2) derives the acceleration from the observed velocity change, measured at a 25 Hz, divided by the pulse duration (1 μs). Applying the same approach to the displacement data in Fig. 5 yields an acceleration of 5×10^5 m/s^2. A slightly higher estimate using the same method is expected corresponding to the higher frame-rate. The lower value obtained from optical flow most likely represents a more physically realistic, time-averaged measure based on continuous centroid tracking, rather than instantaneous approximation.

Cavitation response characterisation

Cavitation activity accompanying each shock wave was quantified from high-speed visible-light images from an imaging axis perpendicular to HSXPCI (Fig. 2). Each frame was first processed with a top-hat filter to enhance local contrast, followed by normalisation and binarization. The projected area of the stone was measured in the first frame and subtracted from all subsequent threshold frames such that only the apparent cavitation activity around the stone periphery was captured. This 2D area projection provides an approximate measure of the bubble cloud's evolution in time. The method assumes that the surface area of the stone remains intact. The ejected stone debris from the sample surface accounts for a small, but non-zero, residual signal in the peripheral cavitation area after approximately 1 ms (Fig. 5).

Surface erosion quantification

The outer surface of the stone was extracted from each reconstructed tomographic volume as a triangulated mesh. Each surface was then converted into a dense point cloud representation where iterative closest point (ICP) alignments were performed between time points to register all datasets to a common reference frame until convergence was achieved. The aligned point clouds were exported to CloudCompare [52], where inter-surface distances were computed using the multiscale model-to-model cloud comparison (M3C2) algorithm [53]. Finally, the resulting distance field was mapped back onto the surface mesh for visualisation (corresponding to red-scale intensity in Fig. 7).

Semantic segmentation

Segmentation of the internal cracks depicted in Fig. 6B and Fig. 8 is performed through Python implementation of the flood-fill method. By initialising a seed to be known within the void, the segmentation region expands until encountering a sharp gradient representative of the stone material interface. This mechanism enables visualisation of specific large fracture regions as displayed in the colourised volumetric representation located within the transparent stone region.

Semantic segmentation (pixel-wise classification) of the complete tomographic datasets are performed in three steps: foreground isolation, stone–fluid segmentation, and water–air segmentation. A strong 3D Gaussian blur ($\sigma_k = 20$) is performed on the entire tomographic dataset to eliminate any background noise, interior porosity, and edge artifacts.

By application of Otsu threshold algorithm within a cylindrical domain (circular crop in x–y plane of radius scale 0.9 the entire reconstructed plane), binary filling, and dilation, the general region in which the stone lies can be masked, thereby isolating the foreground [54]. Once the region of interest (ROI) within the domain is selected, a two-dimensional Gaussian blur ($\sigma_k = 2$) is applied to each x–y slice to minimise noise while preserving edges. Otsu thresholding is performed on the masked foreground to segment stone from fluid pixels.

The total surface area of the stone is determined by summing all interfaces between solid and non-solid pixels (6-connectivity of voxelised representation). Three-dimensional binarized filling ensured that any interior porosity is closed, enabling the exterior surface area to be calculated by the same method. The difference between the total surface area and exterior surface area yields the interior surface area.

The uncertainty of the segmentation is calculated by repeating the Otsu threshold algorithm for an over- and under-estimate of the solid segmentation based on the noise within the ROI (standard deviation, σ). A constant, k, is used to scale the influence of the noise on the threshold value calculated by the Otsu algorithm ($\mu \pm k\sigma$) [55]. The optimal constant to reflect uncertainty within the algorithm, while performing in a range comparable to visual inspection, was determined to be 0.25. Increasing the threshold ($+k\sigma$) corresponds to more conservative material segmentation, leading to greater influence of ring artifacts and uneven lighting in the reconstruction. Lowering the threshold ($-k\sigma$) corresponds to more liberal segmentation of stone pixels, leading to lower interior surface area resulting from filling pores. The influence of adjustment of k relative to the noise within the isolated foreground can be found in Supplementary Information 2.

The damage evolution is calculated by comparing the surface area obtained for each shock wave to the initial state of the same thresholding condition (under-estimate, mean, and over-estimate). Accordingly, the calculated surface area derived from increased threshold ($\mu + k\sigma$) is referenced to the initial under-estimated segmentation region when calculating the percent change. The change, $P_{i,b}$, for each shock wave to the respective baseline, b, can be expressed as the following relation:

$$P_{i,b} = 100 \cdot \left(\frac{SA_{i,b} - SA_{0,b}}{SA_{0,b}}\right),$$

where $SA_{i,b}$ is the surface area for each respective shock and baseline and $SA_{0,b}$ is the initial surface area for each threshold estimate baseline. Inversely, those derived from decreased threshold ($\mu - k\sigma$) are referenced to the initial over-estimated segmentation region. This ensures that the evolution for each shock is evaluated consistently within each uncertainty bound, such that under- and over-estimated trajectories are propagated relative to their respective baseline. The root mean square error of the measurements provides the uncertainty, U_i, of the threshold performance for each shock wave:

$$U_i = \sqrt{\frac{1}{2}((P_{i,b} - P_{i,o})^2 + (P_{i,b} - P_{i,u})^2)},$$

where $P_{i,o}$ and $P_{i,u}$ refer to the over- and under-estimate percent change calculation, respectively.

Finally, the fluid segmented pixels located within the segmented stone volume are classified into air and water through Otsu thresholding. A quantitative analysis regarding fluid within the pores is not implemented in this work, so the uncertainty analysis was not repeated for this step.

DATA AVAILABILITY

Processed datasets underlying the figures and videos, including reconstructed tomographic volumes, segmented volumes, and derived visualisations are provided as Supplementary Information. Full-resolution raw and reconstructed datasets for all scans, including tomographic volumes, segmented volumes, associated metadata, are available from the corresponding author upon reasonable request.

[1] S. R. Khan, M. S. Pearle, W. G. Robertson, G. Gambaro, B. K. Canales, S. Doizi, O. Traxer, and H.-G. Tiselius, Kidney stones, Nature reviews Disease primers **2**, 1 (2016).

[2] M. Sivaguru, J. J. Saw, E. M. Wilson, J. C. Lieske, A. E. Krambeck, J. C. Williams, M. F. Romero, K. W. Fouke, M. W. Curtis, J. L. Kear-Scott, *et al.*, Human kidney stones: a natural record of universal biomineralization, Nature Reviews Urology **18**, 404 (2021).

[3] C. Thongprayoon, A. E. Krambeck, and A. D. Rule, Determining the true burden of kidney stone disease, Nature Reviews Nephrology **16**, 736 (2020).

[4] K. Gillams, P. Juliebø-Jones, S. Ø. Juliebø, and B. K. Somani, Gender differences in kidney stone disease (ksd): findings from a systematic review, Current urology reports **22**, 1 (2021).

[5] J. A. Antonelli, N. M. Maalouf, M. S. Pearle, and Y. Lotan, Use of the national health and nutrition examination survey to calculate the impact of obesity and diabetes on cost and prevalence of urolithiasis in 2030, European urology **66**, 724 (2014).

[6] C. Chaussy, E. Schmiedt, B. Jocham, W. Brendel, B. Forssmann, and V. Walther, First clinical experience with extracorporeally induced destruction of kidney stones by shock waves, The Journal of urology **127**, 417 (1982).

[7] C. Konnopka, B. Becker, C. Netsch, T. R. W. Herrmann, A. J. Gross, L. Lusuardi, T. Knoll, and H. H. König, Long-term evaluation of outcomes and costs of urolithiasis re-interventions after ureteroscopy, extracorporeal shockwave lithotripsy and percutaneous nephrolithotomy based on german health insurance claims data, World Journal of Urology **40**, 3021 (2022).

[8] P. Zhong, Shock wave lithotripsy, in *Bubble Dynamics and Shock Waves*, edited by C. F. Delale (Springer Berlin Heidelberg, Berlin, Heidelberg, 2013) pp. 291–338.

[9] J. E. Lingeman, J. A. McAteer, E. Gnessin, and A. P. Evan, Shock wave lithotripsy: advances in technology and technique, Nature Reviews Urology **6**, 660 (2009).

[10] P. Zhong and G. M. PREMINGER, Mechanisms of differing stone fragility in extracorporeal shockwave lithotripsy, Journal of Endourology **8**, 263 (1994).

[11] W. Eisenmenger, The mechanisms of stone fragmentation in eswl, Ultrasound in medicine & biology **27**, 683 (2001).

[12] O. A. Sapozhnikov, A. D. Maxwell, B. MacConaghy, and M. R. Bailey, A mechanistic analysis of stone fracture in lithotripsy, The Journal of the Acoustical Society of America **121**, 1190 (2007).

[13] T. Leighton and R. Cleveland, Lithotripsy, Proceedings of the Institution of Mechanical Engineers, Part H: Journal of Engineering in Medicine **224**, 317 (2010).

[14] J. J. Rassweiler, T. Knoll, K.-U. Köhrmann, J. A. McAteer, J. E. Lingeman, R. O. Cleveland, M. R. Bailey, and C. Chaussy, Shock wave technology and application: an update, European urology **59**, 784 (2011).

[15] A. M. Loske, *Medical and biomedical applications of shock waves* (Springer, 2017).

[16] C. Chaussy, W. Brendel, and E. Schmiedt, Extracorporeally induced destruction of kidney stones by shock waves, The Lancet **316**, 1265 (1980).

[17] M. Lokhandwalla and B. Sturtevant, Fracture mechanics model of stone comminution in eswl and implications for tissue damage, Physics in Medicine & Biology **45**, 1923 (2000).

[18] A. J. Coleman, J. E. Saunders, L. A. Crum, and M. Dyson, Acoustic cavitation generated by an extracorporeal shockwave lithotripter, Ultrasound in medicine & biology **13**, 69 (1987).

[19] S. Zhu, F. H. Cocks, G. M. Preminger, and P. Zhong, The role of stress waves and cavitation in stone comminution in shock wave lithotripsy, Ultrasound in medicine & biology **28**, 661 (2002).

[20] Y. A. Pishchalnikov, O. A. Sapozhnikov, M. R. Bailey, J. C. Williams Jr, R. O. Cleveland, T. Colonius, L. A. Crum, A. P. Evan, and J. A. McAteer, Cavitation bubble cluster activity in the breakage of kidney stones by lithotripter shockwaves, Journal of endourology **17**, 435 (2003).

[21] W. Sass, M. Bräunlich, H.-P. Dreyer, E. Matura, W. Folberth, H.-G. Priesmeyer, and J. Seifert, The mechanisms of stone disintegration by shock waves, Ultrasound in medicine & biology **17**, 239 (1991).

[22] W. Lauterborn and H. Bolle, Experimental investigations of cavitation-bubble collapse in the neighbourhood of a solid boundary, Journal of Fluid Mechanics **72**, 391 (1975).

[23] Y. A. Pishchalnikov, W. M. Behnke-Parks, K. Schmidmayer, K. Maeda, T. Colonius, T. W. Kenny, and D. J. Laser, High-speed video microscopy and numerical modeling of bubble dynamics near a surface of urinary stone, The Journal of the Acoustical Society of America **146**, 516 (2019).

[24] C. Lechner, W. Lauterborn, M. Koch, and R. Mettin, Jet formation from bubbles near a solid boundary in a compressible liquid: Numerical study of distance dependence, Physical Review Fluids **5**, 093604 (2020).

[25] F. Reuter and C.-D. Ohl, Supersonic needle-jet generation with single cavitation bubbles, Applied Physics Letters **118** (2021).

[26] A. Philipp and W. Lauterborn, Cavitation erosion by single laser-produced bubbles, Journal of fluid mechanics **361**, 75 (1998).

[27] O. Supponen, D. Obreschkow, P. Kobel, M. Tinguely, N. Dorsaz, and M. Farhat, Shock waves from nonspherical cavitation bubbles, Physical Review Fluids **2**, 093601 (2017).

[28] T. Trummler, S. H. Bryngelson, K. Schmidmayer, S. J. Schmidt, T. Colonius, and N. A. Adams, Near-surface dynamics of a gas bubble collapsing above a crevice, Journal of Fluid Mechanics **899**, A16 (2020).

[29] L. A. Crum, Cavitation microjets as a contributory mechanism for renal calculi disintegration in eswl, The Journal of urology **140**, 1587 (1988).

[30] R. O. Cleveland and J. van Cauweleart, Fragmentation mechanisms of kidney stones in shock wave lithotripsy can be detected with microct x-ray imaging, in *Proceedings of the Joint German Convention on Acoustics and Congrès Francais d'Acoustique CFA, Strasbourg, France* (2004) pp. 981–982.

[31] J. Field, The physics of liquid impact, shock wave interactions with cavities, and the implications to shock wave lithotripsy, Physics in Medicine & Biology **36**, 1475 (1991).

[32] O. J. Wess and J. Mayer, Fragmentation of brittle material by shock wave lithotripsy. momentum transfer and inertia: a novel view on fragmentation mechanisms, Urolithiasis **48**, 137 (2020).

[33] R. O. Cleveland, J. A. McAteer, and R. Müller, Time-lapse nondestructive assessment of shock wave damage to kidney stones in vitro using micro-computed tomography, The Journal of the Acoustical Society of America **110**, 1733 (2001).
[34] J. A. McAteer, J. C. Williams, R. O. Cleveland, J. Van Cauwelaert, M. R. Bailey, D. A. Lifshitz, and A. P. Evan, Ultracal-30 gypsum artificial stones for research on the mechanisms of stone breakage in shock wave lithotripsy, Urological research **33**, 429 (2005).
[35] K. Xiang, L. Qin, S. Huang, H. Song, V. Bazhenov, V. Bellucci, S. Birnšteinová, R. de Wijn, J. C. P. Koliyadu, F. H. M. Koua, A. Round, E. Round, A. Sarma, T. Sato, M. Sikorski, Y. Zhang, E. M. Asimakopoulou, P. Villanueva-Perez, K. Porfyrakis, I. Tzanakis, D. G. Eskin, N. Grobert, A. P. Mancuso, R. Bean, P. Vagovič, and J. Mi, Ultrasonic cavitation shock wave exfoliation dynamics of 2d materials revealed in situ by mhz xfel imaging and multiphysics modeling, Science Advances **11**, 1 (2025).
[36] G. Su, M. Gotthardt, and M. Gollasch, Assessment of nanoindentation in stiffness measurement of soft biomaterials: kidney, liver, spleen, and uterus, Scientific reports **10**, 18784 (2020).
[37] V. Popov, *Contact Mechanics and Friction: Physical Principles and Applications*, Vol. 55 (Springer Link, 2010).
[38] K. Schmidmayer, G. T. Bokman, A. Sieber, A. Ade-Onojobi, B. Lukic, G. Shakya, A. Kühl, M. Schlötter, M. Belau, and O. Supponen, Exploring the interplay of stone-attached and distant cavitation bubbles during extracorporeal shock wave lithotripsy, in *ICMF 2025-12th International Conference on Multiphase Flow* (2025).
[39] R. O. Cleveland and J. A. McAteer, Physics of shock-wave lithotripsy, in *Smith's Textbook of Endourology* (Blackwell Publishing Ltd, 2012) pp. 317–332.
[40] B. Hopkinson, A method of measuring the pressure produced in the detonation of high explosives or by the impact of bullets., Proceedings of the Royal Society of London **89**, 411 (1918).
[41] A. D. Maxwell, B. MacConaghy, M. R. Bailey, and O. A. Sapozhnikov, An investigation of elastic waves producing stone fracture in burst wave lithotripsy, The Journal of the Acoustical Society of America , 1607 (2020).
[42] J. C. Simon, O. A. Sapozhnikov, W. Kreider, M. Breshock, J. C. Williams, and M. R. Bailey, The role of trapped bubbles in kidney stone detection with the color doppler ultrasound twinkling artifact., Physics in medicine and biology **63**, 025011 (2018).
[43] J. C. Simon, J. R. Holm, J. Thiel, B. Dunmire, B. W. Cunitz, and M. R. Bailey, Evidence of microbubbles on kidney stones in humans, Ultrasound in Medicine and Biology **46**, 1802 (2020).
[44] R. O. Cleveland and J. S. Tello, Effect of the diameter and the speed of sound of a kidney stone on the acoustic field induced by shock waves, Acoustic Research Letters Online **5**, 37 (2004).
[45] Z. Ren, Z. Zuo, S. Wu, and S. Liu, Particulate projectiles driven by cavitation bubbles, Physical review letters **128**, 044501 (2022).
[46] A. Evan, F. Coe, J. Lingeman, Y. Shao, A. Sommer, S. Bledsoe, J. Anderson, and E. Worcester, Mechanism of formation of human calcium oxalate renal stones on randall's plaque, The Anatomical Record **290**, 1315 (2007).
[47] A. M. Loske, *Shock wave physics for urologists* (UNAM, Centro de Física Aplicada y Tecnología Avanzada, 2007).
[48] D. Zhang, S. Li, Z. Zhang, N. Li, X. Yuan, Z. Jia, and J. Yang, Urinary stone composition analysis and clinical characterization of 1520 patients in central China, Scientific reports **11** (2021).
[49] Y. Chou, C. Huang, W. Li, S. Huang, W. Wu, C. C. Tsai, A. Chang, S. Chen, Y. Lin, and L. Y.P., Clinical study of ammonium acid urate urolithiasis, Kaohsiung Journal of Medical Sciences , 259 (2012).
[50] G. T. Bokman, L. Biasiori-Poulanges, B. Lukić, C. Bourquard, D. W. Meyer, A. Rack, and O. Supponen, High-speed x-ray phase-contrast imaging of single cavitation bubbles near a solid boundary, Physics of Fluids **35** (2023).
[51] H. J. Woltring, A fortran package for generalized, cross-validatory spline smoothing and differentiation, Advances in Engineering Software **8**, 104 (1986).
[52] D. Girardeau-Montaut, Cloudcompare (version 2.13.2) [gpl software], `http://www.cloudcompare.org/` (2024).
[53] D. Lague, N. Brodu, and J. Leroux, Accurate 3d comparison of complex topography with terrestrial laser scanner: Application to the rangitikei canyon (n-z), ISPRS Journal of Photogrammetry and Remote Sensing **82**, 10 (2013).
[54] N. Otsu, A threshold selection method from gray-level histograms, IEEE Transactions on Systems, Man, and Cybernetics **9**, 62 (1979).
[55] M. C. Krygier, T. LaBonte, C. Martinez, C. Norris, K. Sharma, L. N. Collins, P. P. Mukherjee, and S. A. Roberts, Quantifying the unknown impact of segmentation uncertainty on image-based simulations, Nature Communications **12**, 5414 (2021).

ACKNOWLEDGEMENTS

The authors recognise Luc Biasiori-Poulanges for the initial conceptualisation of this experimental campaign, and we acknowledge the European Synchrotron (ESRF) for providing the necessary synchrotron radiation facilities and the beamline ID19 (Proposal ME-1663). For assistance in X-ray powder diffraction analysis, we thank Ma Ning from the Institute of Geochemistry and Petrology (ETH Zürich). We acknowledge the role of Herwig Requardt in coordinating logistics of the experimental setup and assisting with device installation. K.S. acknowledges support from ANR-24-CE51-0508-01.

AUTHOR CONTRIBUTIONS

O.S., B.L., G.S., K.S. and A.S. conceived the research. A.S., B.L., G.S., G.T.B., A.K., M.S., and K.S. performed experimentation. A.S. and C.B. drafted the initial manuscript with the help of all authors. A.S. and C.B. wrote the image processing code. A.K., M.B., A.S., and G.S. designed the experimental setup. A.S., C.B., B.L., and K.S. participated in data analysis. This research was conducted under the supervision of O.S. and M.B., and A.S. and C.B. contributed equally to this work.

COMPETING INTERESTS

A.K., M.S., and M.B. are employees at Storz Medical. The authors declare no competing interests.

SUPPLEMENTARY INFORMATION

Supplementary information is available for this paper and includes:

- **Supplementary Information 1:** X-ray powder diffraction (XRD) profile.
- **Supplementary Information 2:** Segmentation uncertainty visualisation.
- **Supplementary Information 3:** Cavitation energy estimation.
- **Supplementary Video 1:** High-speed optical imaging (Photron Nova) and High-speed X-ray phase-contrast imaging (Photron SA-Z) acquired during treatment for both stones.
- **Supplementary Video 2:** Background subtracted high-speed dynamic fracture video (Shimadzu) with labelled damage mechanisms.
- **Supplementary Video 3:** Rotating 3D volume renderings for AAU treatment.
- **Supplementary Video 4:** Rotating 3D volume renderings for COM treatment.

All supplementary videos are provided using standard H.264 encoding with 16:9 aspect ratio and are intended to support qualitative interpretation of the experimental results presented in the main text.

Correspondence and requests for materials should be addressed to Cameron Brewer or Outi Supponen.

Supplementary Files

This is a list of supplementary files associated with this preprint. Click to download.

- SupplementaryCode.zip
- SupplementaryInformation.pdf
- SupplementaryVideo2.mp4
- SupplementaryVideo3.mp4
- SupplementaryVideo4.mp4
- SupplementaryVideo1.mp4